*Invited Paper*

# Microfabricated Planar Helical Slow-Wave Structures Based on Straight-Edge Connections for THz Vacuum Electron Devices

Ciersiang Chua [1, 2], Sheel Aditya [1*], Julius M. Tsai [2], Min Tang [2], and Zhongxiang Shen [1]
[1] School of Electrical and Electronic Engineering, Nanyang Technological University, Singapore 639798.
[2] Institute of Microelectronics, A*STAR (Agency for Science, Technology and Research), Singapore
[*]Email: ESAditya@ntu.edu.sg

(Received September 14, 2011)

**Abstract:** This paper reports on two planar helical slow-wave structures that offer wide bandwidth and a good potential for microfabrication. The paper begins with a review of progress made in recent years in the development of a planar helix slow-wave structure with straight-edge connections (PH-SEC). This is followed by new results that compare the performance of the PH-SEC with that of the circular and rectangular tape helices; specially considered is the interaction impedance for the forward- and backward-wave. The focus of the rest and the major part of the paper is a new slow-wave structure, namely, the rectangular ring-bar with straight-edge connections (RRB-SEC). It is shown that, similar to the case of the circular ring-bar structure, the RRB-SEC enhances the interaction impedance for the fundamental forward-wave while reducing the interaction impedance for the backward-wave. Detailed results for phase velocity and interaction impedance of the RRB-SEC are presented to show the effect of structure dimensions. Two configurations which are suitable for microfabrication of the RRB-SEC on a silicon wafer are also presented. As a proof-of-concept, one of these configurations, designed for operation at W-band, is microfabricated. The fabricated structures include a coplanar waveguide feed. On-wafer cold-test *S*-parameter measurements are reported for frequencies from 80 to 110 *GHz*. The measured results match well with the simulation results when the effect of surface roughness of the different parts of the fabricated structures is accounted for in the simulations. The RRB-SEC, with rectangular or square cross section, has potential application in high frequency travelling-wave tubes that aim to achieve high power operation.

**Keywords**: Electron devices, Interaction impedance, Phase velocity, Planar helix, Ring-bar, Slow-wave structure, Traveling-wave tube.

**doi:** 10.11906/TST.208-229.2011.12.25

## 1. Introduction

Development of medical imaging, spectroscopy, and high-altitude telecommunication relies on availability of high efficiency terahertz sources. In recent years, there has been an increasing interest in travelling-wave tubes (TWTs) as well as other vacuum electron devices (VEDs) operating at millimeter-wave (30 *GHz*-300 *GHz*) and submillimeter-wave (300 *GHz*-3 *THz*) frequencies. Since the conventional fabrication techniques become inadequate at these frequencies, microfabrication technology is crucial for VEDs operating at these frequencies [1]. An additional benefit of the microfabrication technology would be to reduce the cost through mass production [2].

With regard to high frequency VEDs, microfabrication of several slow-wave structures (SWSs) has been reported in the literature. Table 1 provides a brief summary of the various microfabricated SWSs for THz VEDs in the last decade. In general, folded waveguide [3-5], coupled cavity [6-8], vane loaded waveguide [9], [10], and corrugated waveguide [11] structures are formed completely by metal and their RF operation does not involve dielectric loading. These structures can handle higher output power due to superior thermal dissipation capability and large

Tab. 1 SUMMARY OF VARIOUS RECENT MICROFABRICATED SWSS FOR THZ VEDS

| SWS | Primary author | Year | Frequency | Main Processes | Photoresist |
|---|---|---|---|---|---|
| Folded waveguide | S. Bhattacharjee [3] | 2004 | 400 *GHz* | X-ray LIGA; UV LIGA; DRIE | PMMA; SU-8 |
| | Y. M. Shin [4] | 2006 | 100 *GHz* | X-ray LIGA | PMMA |
| | R. Zheng [5] | 2010 | 220 *GHz* | UV LIGA | SU-8 |
| Coupled Cavity | Y. M. Shin [6] | 2003 | 95 *GHz* | X-ray LIGA | PMMA |
| | C. W. Baik [7] | 2008 | 100 *GHz* | DRIE | Details not given |
| | O. Kwon [8] | 2010 | 100 *GHz* | X-ray LIGA | PMMA |
| Vane loaded waveguide | L. Earley [9] | 2006 | 94 *GHz* | EDM | Not applicable |
| | Y. M. Shin [10] | 2009 | 220 *GHz* | UV LIGA; DRIE | KMPR (UV LIGA) |
| Double corrugated waveguide | C. Paoloni [11] | 2011 | 0.3-2 *THz* | UV LIGA | SU-8 |
| Raised meander-line | S. Sengele [12] | 2009 | W-band | DRIE and UV LIGA | AZ1827, AZ 5214E |
| Biplanar interdigital | M. R. Lueck [13] | 2011 | 650 *GHz* | CVD, DRIE and UV LIGA | Dry film |
| Circular helix (Octagonal; square) | J. A. Dayton [14]<br>M. R. Lueck [13] | 2009<br>2011 | 95 *GHz*;<br>650 *GHz* | CVD, RIE and UV LIGA | Details not given |
| Planar helix | C. Chua [15] | 2011 | W-band | Lift-off and UV LIGA | MaN-1440, AZ 40XT-11D, dry film |

transverse dimensions. On the other hand, meander-line [12] and planar helix [15] structures involve dielectric loading; these structures have low to moderate power handling capability due to low thermal dissipation capability. In addition to these characteristics, some other distinctive features of these structures are as follows: the folded waveguide structure offers larger bandwidths (20-30%) than that for the coupled-cavity structure (10-15%); the coupled-cavity structure offers higher interaction impedance than the folded waveguide structure; the staggered double vane-loaded waveguide structure offers ~30% bandwidth; the double corrugated waveguide structure offers a strong interaction with a cylindrical beam; the raised meander-line structure has higher interaction impedance and lower attenuation compared to the simple meander-line structure; the structures built by patterning of diamond-biplanar interdigital [13] and circular helix [13] and [14] - enjoy excellent thermal dissipation, moderate dielectric loading, high dielectric strength and low loss. Finally, the structures that are close relatives of the circular helix offer wide bandwidths.

Semiconductor device fabrication involves steps like photolithography and chemical etching for pattern transfer of two-dimensional integrated circuitries. Microfabrication adapts the semiconductor device fabrication technologies to fabricate three-dimensional micromachined electromechanical systems (MEMS), such as pressure sensors, accelerometers and gyros [16]. Microfabrication has also been applied to fabricate radiofrequency (RF), biomedical, and optical devices. Various techniques, such as lithography, electroplating, and micro-molding (LIGA), deep reactive ion-etching (DRIE), electrical discharge machining (EDM) etc., have been established for producing three-dimensional structures suitable for high frequency VEDs [17].

LIGA is the most popular process for fabrication of the structures listed in Table 1. This process involves molding and electroplating. The advancement of material research has brought on a wide range of photoresists which do not rely on large and expensive x-ray synchrotron facility. As an example, SU-8 can be patterned using low-cost UV light and one can produce high

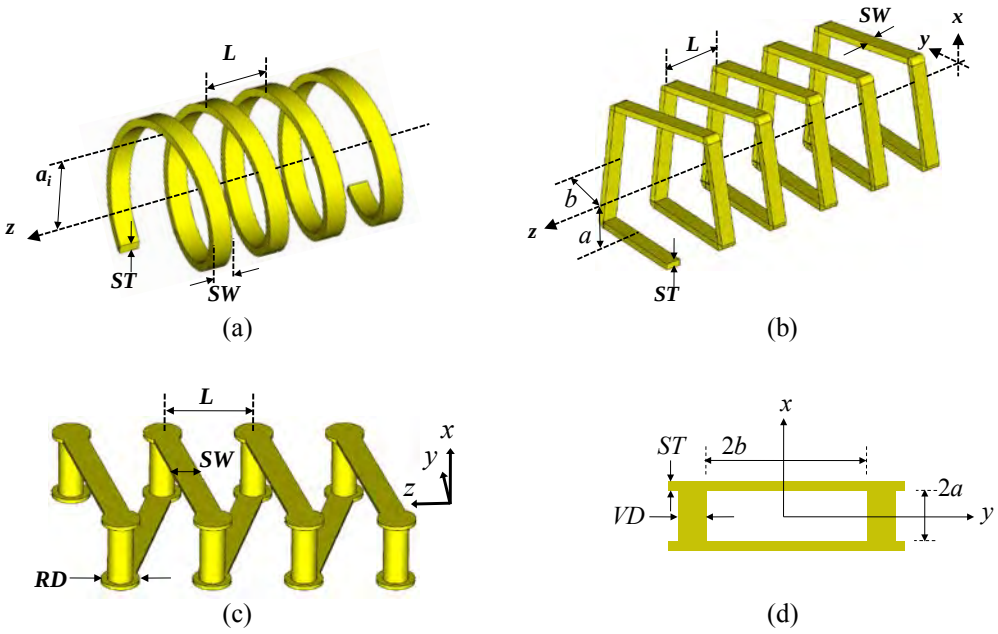


Fig. 1 Perspective view of (a) circular tape helix, (b) rectangular (or square) tape helix and (c) PH-SEC with cylindrical via structures immersed in free space. (d) The cross-sectional view of PH-SEC with cylindrical via.

aspect ratio structures which are required for millimeter-wave frequency range. Since the crosslinked SU-8 is difficult to remove after electroplating, other UV sensitive photoresists, such as KMPR [10] and AZ 40XT-11D [15], have been reported to replace SU-8. Unlike the all metal structures, the structures that involve dielectric loading normally require more fabrication steps due to multi-level metallization. Currently, several factors remain as key challenges for fabricating THz VEDs, such as bonding of two halves of the circuits, reducing the surface roughness, reducing the processing time, and packaging of complete devices.

Among the various SWSs proposed for TWTs, the circular helix holds a unique position due to its capability for strong electron-wave interaction over large bandwidths. However, the circular shape is difficult to realize faithfully in microfabrication and may need to be approximated as octagonal or square [14]. Thus, a few SWSs that are closely related to the circular helix have been proposed in the literature. In general, the fabrication of helix-like structures has less stringent alignment issues due to their broadband nature [13]. Figures 1 (a)-(c) show the perspective view of the circular tape helix, rectangular (or square) tape helix, and PH-SEC with cylindrical vias immersed in free space. For miniaturization and sheet beam application, one prefers planar structures. The PH-SEC [18] can be considered to be derived from a pair of parallel unidirectionally conducting (UC) screens [19] and [20], or from the rectangular helix [21]. The PH-SEC retains the broad bandwidth feature of the conventional circular helix. Unlike the rectangular or the circular helix, the straight-edge connections can be realized easily using microfabrication techniques. In fact, the PH-SEC can be realized quite faithfully using the microfabrication processes [15]. In addition, as shown in Fig. 1 (d), the PH-SEC can have a rectangular cross-sectional geometry which is suitable for interaction with a sheet electron beam. Sheet beam devices offer advantages such as higher beam current capacity, decreased beam voltage, and lower magnetic field strength [22-24]. Other planar structures reported in [9], [10], [12], [13], and [24] may also be suitable for interaction with a sheet electron beam; however, the

helix-based structures offer larger operating bandwidths.

Although the helix SWS has the advantage of wide bandwidth, its application has been limited to relatively low power TWTs. For high power applications, the beam voltage is required to be high (> 5 *kV*). For velocity synchronism, this corresponds to a helix with a large pitch angle. Under such conditions, (i) the interaction impedance of the fundamental forward-wave mode is reduced due to non-interacting space harmonics, and (ii) the interaction impedance of the backward-wave mode is increased. These effects may result in oscillation [25]. Chodorow and Chu [25] proposed in 1955 the cross-wound twin helix to overcome the difficulties of a single tape helix. In 1956, Birdsall and Everhart [26] proposed the circular ring-bar structure as a practical form of the cross-wound twin helix. When it comes to high power applications, as shown in Section 2, the PH-SEC also suffers from similar problems as the circular helix. To address these problems, we propose here a new structure, a rectangular ring-bar with straight-edge connections (RRB-SEC); we consider the square shape as a special case of the rectangular shape. Analogous to the circular ring-bar, the new structure has the potential to enable high power operation of planar TWTs operating at millimeter-wave and higher frequencies.

In the rest of the paper, we first review the recent work and also present new results for the PH-SEC. Then we present a detailed study of the properties of the RRB-SEC structure. The paper is organized as follows. Section 1 gives a brief summary of the various SWSs for TWTs that have been microfabricated in recent years. The significance of the planar SWSs based on the helical shape is also mentioned. In Section 2, we review the simulation results for the dispersion characteristics and interaction impedance of the PH-SEC, for both square and rectangular cross sections, and compare these parameters with those for the circular and rectangular tape helix, all structures immersed in free space. Particular attention is paid to the interaction impedance for the forward- and backward-wave. In Section 3, we first compare the simulated dispersion characteristics and interaction impedance for the RRB-SEC with those for the circular ring-bar, circular helix and PH-SEC with a view to assess the suitability of the RRB-SEC for high power applications. Next, we study in detail the effects of structure dimensions on the properties of the RRB-SEC. Section 3 concludes with a description of two RRB-SEC configurations that can be microfabricated on a silicon wafer. In Sections 2 and 3, the simulation results for phase velocity and interaction impedance are obtained using the CST eigenmode solver. In Section 4, we provide proof-of-concept microfabrication and measurement results at W-band for the simpler of the two RRB-SEC configurations on silicon. Included are the design of a coplanar waveguide (CPW) feed and the steps for microfabrication. The on-wafer cold-test measured *S*-parameters, covering the 80-110 *GHz* frequency range, are also presented in this section. The measured results are compared with the simulation results obtained using the CST Microwave Studio transient solver; the effects of surface roughness and contact resistance are accounted for in the simulations by estimating effective conductivity of different parts of the microfabricated structures. The paper ends with a summary of important conclusions in Section 5.

## 2. PH-SEC

In this section, we first review the distinctive features of the PH-SEC with reference to the circular helix and rectangular helix. Then, we study the effect of large pitch angle of the PH-SEC

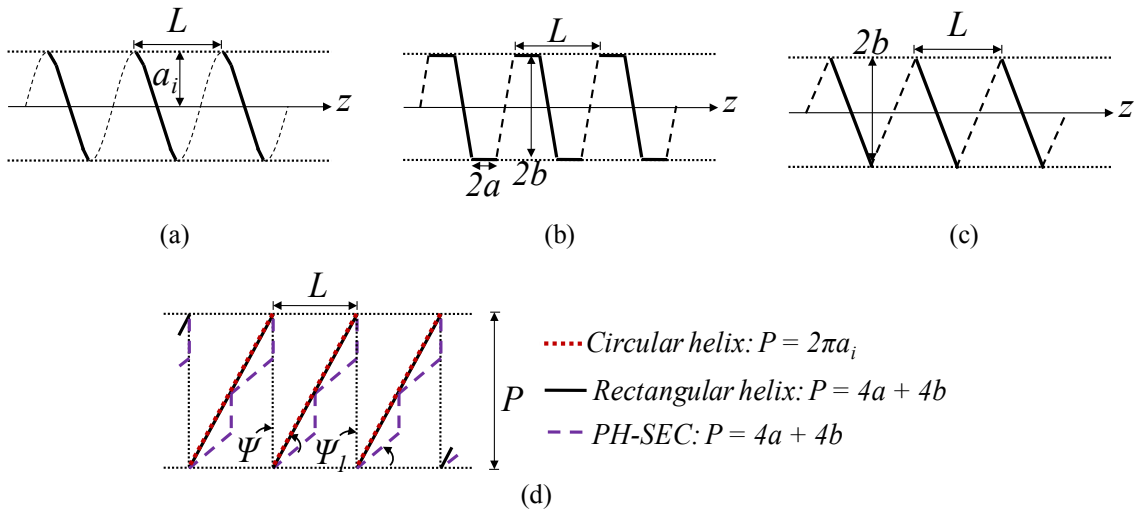


Fig. 2 Plan view of idealized (a) circular helix, (b) rectangular helix and (c) PH-SEC in free space. (d) Unfolded view of the corresponding helices.

on the phase velocity and interaction impedance for the fundamental forward and backward waves. The dispersion characteristics of the PH-SEC immersed in free space, obtained using the effective dielectric constant (EDC) method, have been reported in [18]. In the EDC method, the original 3D waveguide is replaced by two related 2D structures that are easy to analyze. Subsequently, the PH-SEC has been studied for application in TWTs and the effects of several practical modifications to the basic structure have been examined in [27]. These modifications comprise a vacuum tunnel, metal shield, and multilayer dielectric substrates. A modified effective dielectric constant (MEDC) method has been proposed to obtain the dispersion characteristics for different possible configurations. Further, interaction impedance for the different configurations has been calculated using the corresponding 2D approximations. Effects of variations in aspect ratio, metal shield distance, and dielectric constant of the substrates on phase velocity and interaction impedance have been studied. It has been demonstrated that a reasonably flat phase velocity versus frequency curve can be obtained by selecting a proper set of dimensional and material parameters. A possible method of printed circuit board fabrication and a method of making input or output connections using CPW feed have been described in [27] and [28]. The performance of the PH-SEC with a sheet electron beam at C-band has also been estimated using the CST Particle-In-Cell (PIC) solver [29].

As a part of the European project "OPTHER", PIC simulation results for a helical structure on quartz substrate, with CPW feed and cylindrical electron beam at 850 *GHz*, have been reported [30] and [31]. Although the helical structure is called a square helix in these papers, the structure appears identical to the PH-SEC described in [27] and [28]; however, no microfabrication results are reported. Recently, we have demonstrated the microfabrication of a W-band PH-SEC on a silicon substrate using a UV LIGA process [15]. The on-wafer cold-test measurement results have also been presented in detail [32]. Effective conductivity values, incorporating the effect of surface roughness, have been obtained for different metal layers in the fabricated structures.

As shown in the plan view in Fig. 2 (a), a circular helix with a certain radius $a_i$ can be considered to be obtained by winding a conducting wire or tape in a helical fashion on a circular

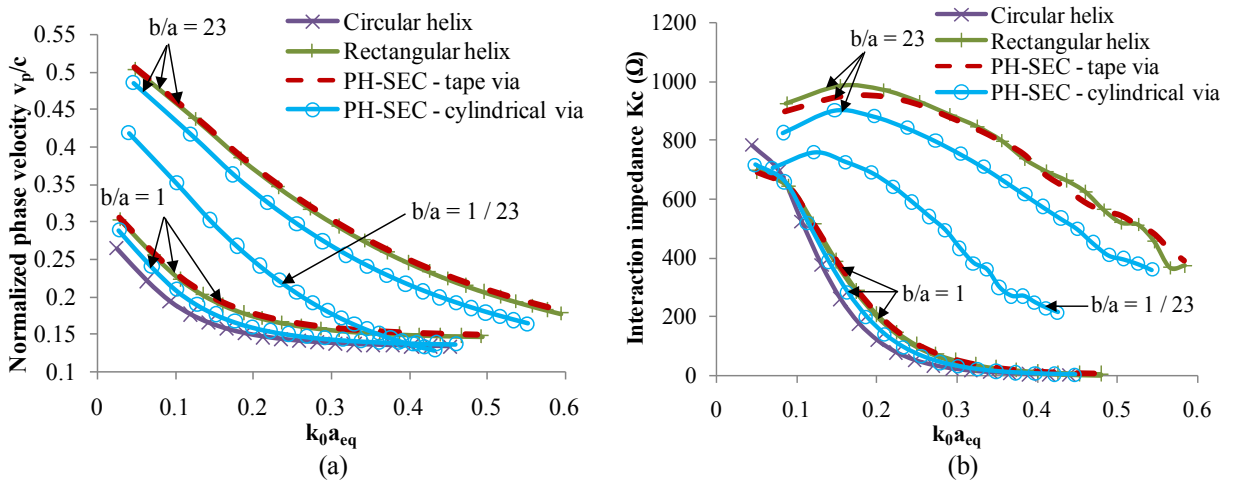


Fig. 3 Simulated (a) normalized phase velocity and (b) interaction impedance for circular helix, rectangular helix and PH-SEC for $b$ / $a$ = 1, 23 and 1 / 23 with fixed $P$ and $L$.

cylinder. Similarly, a rectangular helix, as shown in Fig. 2 (b), can be obtained by replacing the circular cylinder by a rectangular cylinder of cross-section width $2b$ and height $2a$. In the rectangular helix, the connections between any two opposite sides require inclined conductors. The PH-SEC, as shown in Fig. 2 (c), is also obtained using a rectangular cylinder; however, in this case, the inclined conductors in the vertical direction are replaced by straight connections. Due to the straight-edge connections in the PH-SEC, the parts of length $2a$ are not visible in the 2D views.

The unfolded views of the circular helix, rectangular helix and PH-SEC are shown in Fig. 2(d). As seen in Fig. 2 (d), for a fixed period $L$ and fixed cross section perimeter $P$, the pitch angle for PH-SEC, $\Psi_1$, is greater than the pitch angle for both circular and rectangular helices, $\Psi$, since the straight-edge connections have $0^0$ pitch angles. $\Psi_1$ and $\Psi$ have the following relationship:

$$\tan\psi = \frac{b}{a+b}\tan\psi_1 \tag{1}$$

For a given PH-SEC, (1) can be used to calculate an equivalent value of the pitch angle $\Psi$ for a corresponding rectangular or circular helix. Since the pitch angle $\Psi$ is related to phase velocity, it can be seen that the phase velocity of the PH-SEC is less than or equal to that for a rectangular helix with identical cross-sectional perimeter and equal inclination of the parts with length $2b$; the phase velocity of the PH-SEC decreases monotonically as one moves from the case of large $b$ values to small $b$ value.

Figure 3 shows a comparison of the phase velocity and interaction impedance between the circular tape helix, rectangular tape helix and PH-SEC. For the PH-SEC, the realization of straight-edge connections using vias in the shape of both cylindrical or tape are considered. Referring to Fig. 1, the cross section circumference for the circular tape helix is defined using the inner radius $a_i$ of the tape. Similarly, the cross-section perimeter for the rectangular tape helix and PH-SEC is defined using the inner width $2b$ and height $2a$. While a metal shield is included in the structures that are used for simulations, we assume that the metal shield is far away from the

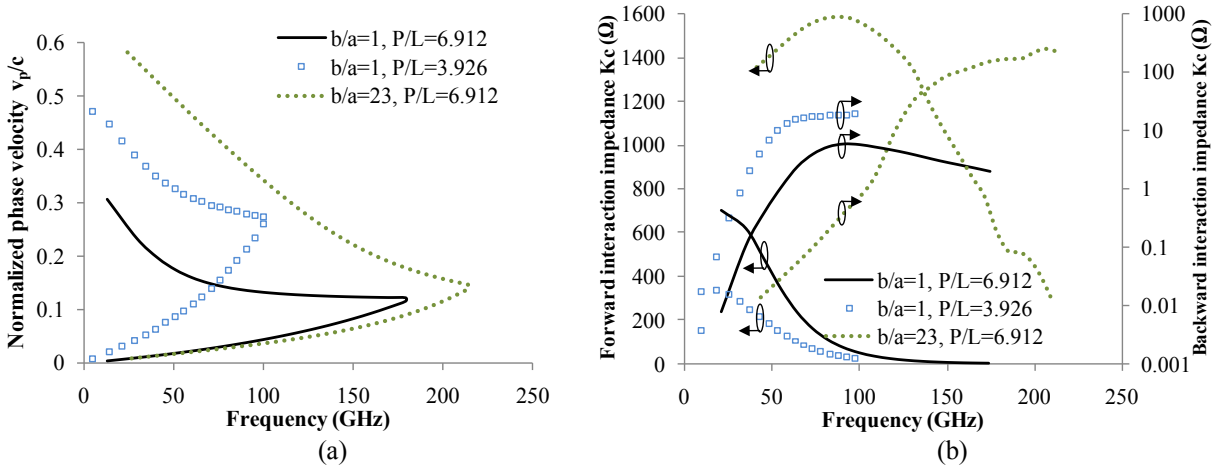


Fig. 4 Simulated (a) normalized phase velocity and (b) interaction impedance for the PH-SEC with cylindrical vias for the fundamental forward and backward waves for different $P/L$.

structures so that, effectively, the structures are immersed in free space. In addition, in Fig. 3, the cross-section perimeter $P$, period $L$, tape width $SW$ and tape thickness $ST$ are assumed to be the same for all structures. Unlike the circular helix, the rectangular helix and PH-SEC can have the freedom of different aspect ratios $b/a$. The detailed dimensions of each structure are listed in Table 2 in the Appendix. The frequency is normalized using an equivalent radius $a_{eq}$. For square and rectangular geometries, $a_{eq}$ is $P / 2\pi$; for the circular geometry, $a_{eq}$ is the inner radius $a_i$. We first compare the circular helix with the case of a square cross section ($b/a$ = 1). All the results in this category are close to each other with only minor differences since the period and cross section perimeter are the same for the three structures. The circular helix offers the flattest phase velocity, but the interaction impedance is the lowest. The phase velocity of the rectangular helix is identical to that for the PH-SEC with tape vias, and is higher than that of the other structures. The square cross section tends to have a slightly higher phase velocity than that for the circular cross section; this is attributed to coupling of the fields near the right angle bends for the square geometry. For the PH-SEC with cylindrical vias, due to the vias and the ring pads (see Fig. 1(c)), the 'effective perimeter' is greater than that for the tape vias; this leads to a slightly lower phase velocity for the case of cylindrical vias.

In general, as the aspect ratio increases, the frequency range of operation increases and the interaction impedance improves significantly for the rectangular helix and the PH-SEC since the helical arms are brought closer to the axis of the structure. Figure 3 shows these results for $b/a$ = 23. Further, unlike the rectangular helix, for the PH-SEC the phase velocity and interaction impedance for $b/a$ = 23 and 1/23 are different since the proportion of straight-edge parts is quite different in the two cases. For $b/a$ = 1/23, the straight-edge connections at the two ends of a helical arm are very close to each other and carry currents in opposite directions. Hence, there is a strong coupling between these straight-edge connections, resulting in a higher dispersion and lower interaction impedance.

Next, we pay attention to the phase velocity and interaction impedance for the PH-SEC with cylindrical vias for the fundamental forward wave and backward wave modes. Figure 4 shows a comparison of these parameters for different values of the cross section perimeter to period ratio

*P*/*L*. The detailed dimensions of each structure are listed in Table 2 in the Appendix. To facilitate comparison, the phase velocity values of the backward wave mode are also plotted in the positive quadrant. The axis for the backward-wave interaction impedance is plotted on log scale so as to cover a large range of values. For the first case, with $b/a = 1$ and $P/L = 6.912$, the normalized phase velocity for the forward-wave is 0.139 at 85 *GHz*. In the second case, the $b/a$ is maintained at 1 and $P/L$ is lowered to 3.926 in order to achieve a higher normalized phase velocity of 0.283 at 85 *GHz*. In the second case, the interaction impedance for the fundamental forward wave is reduced and the interaction impedance for the backward wave is increased. These effects show that the PH-SEC with square cross-section and large pitch angles may be prone to oscillations. In the third case, $b/a$ is changed to 23 but *P* and *L* dimensions are identical to those for the first case. In this case, the normalized forward-wave phase velocity at 85 *GHz* is the highest at 0.38, the interaction impedance of the forward wave is increased significantly and, below ~110 *GHz*, the interaction impedance of the backward wave component is the lowest among the three cases. At 85 *GHz*, the ratio of the impedance for the backward-wave and forward-wave is around 5 % and 0.02 % for the first and the third case, respectively. However, it shoots up to 40 % for the second case.

## 3. RRB-SEC

In Section 1, it was mentioned that the circular ring-bar structure was proposed to ease the difficulties encountered in using the circular helix for high power operation [25-26]. The results for dispersion characteristics and interaction impedance of the circular ring-bar structure have been reported extensively [25], [33-36]. In the early days, the fabrication of the circular ring-bar involved saw-cutting of a hollow molybdenum tube [26]. To increase the operating frequency, lithography and etching on hollow preform have been reported [37-38]. Expensive laser cutting of molybdenum cylinder has also been reported [39]. However, to the best of the authors' knowledge, the fabrication schemes reported in the literature can only produce the ring-bar structures for operation well below 100 *GHz*. In addition, the circular cross section of the ring-bar structure implies operation with a cylindrical electron beam.

In Section 2, the limitations of the PH-SEC with square cross-section for high power application have also been brought out. In this section, we describe in detail a novel RRB-SEC structure, which is shown in Fig. 5 (a). The RRB-SEC is motivated by the circular ring-bar structure [26] which is shown in Fig. 5 (b) and is a practical form of the cross-wound twin helices. In the symmetric waveguide mode of the cross-wound twin helices, the axial electric fields of the fundamental forward wave modes in the two helices combine and result in a high value of the axial interaction impedance; the space harmonics carry mainly the magnetic energy and result in low interaction impedance for the backward-wave [25]. The RRB-SEC is a planar version of the circular ring-bar structure and can be suitable for sheet beam applications. In this section, we study several interesting properties of the RRB-SEC in free space and the RRB-SEC in the presence of a silicon substrate. In sub-section 3.1, the simulated dispersion characteristics and interaction impedance of the RRB-SEC are compared with those for the circular helix, circular ring-bar and PH-SEC. In sub-section 3.2, detailed results are presented to show the effect of dimensional parameters. Sub-section 3.3 describes two configurations that are suitable for microfabrication on a silicon wafer.

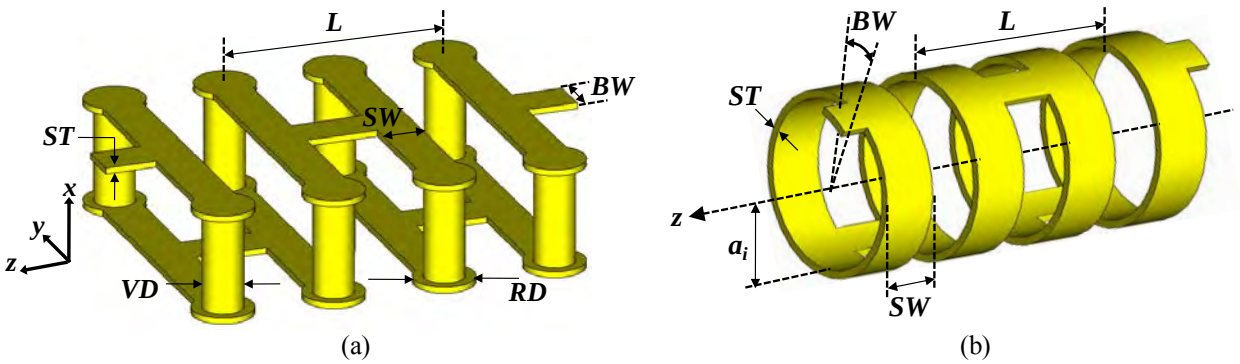


Fig. 5 Perspective view of (a) RRB-SEC with cylindrical via and (b) circular ring-bar structures immersed in free space.

The RRB-SEC, as shown in Fig. 5 (a), consists of three metal layers - the bottom horizontal layer, the top horizontal layer, and the vertical straight-edge connections (or vias) that connect the two horizontal layers. The top and bottom horizontal layers consist of conducting strips, oriented along the *y*-direction, with thickness *ST* and width *SW*. Adjacent conducting strips are joined by a conducting bar oriented along the *z*-direction, with thickness *ST* and width *BW*. The conducting bars are analogous to the crossover (overlapping) of the cross-wound twin helices. Each cylindrical via has a diameter *VD* and it connects the top and bottom ring pads which have a diameter *RD* (> *VD*). A rectangular ring is formed by the top and bottom conducting strips and the two vias at the edges of the metal strips. *L* is the period of the structure. The center to center distance between two adjacent rectangular rings is *L* / 2. The cross section dimensions of the RRB-SEC along the *x*- and *y*-directions are 2*a* and 2*b*, respectively, similar to that for the PH-SEC in Fig. 1 (d). The center of the rectangular rings coincides with (0, 0). For the circular ring-bar structure shown in Fig. 5 (b), the inner radius and bar width (arc length) are denoted as $a_i$ and *BW*.

### 3.1 Comparison of RRB-SEC with circular helix, circular ring-bar, and PH-SEC

Figure 6 shows the phase velocity and interaction impedance of the circular helix, circular ring-bar and RRB-SEC, with *b*/*a* = 1, 23 and 1/23. The RRB-SEC is considered with both cylindrical vias and tape vias. We assume that the metal shield, used in simulations, is far away from the structures so that, effectively, the structures can be considered to be immersed in free space. In addition, *P*, *L*, *SW*, *ST* and *BW* are the same for all the structures. The detailed dimensions of each structure are listed in Table 2 in the Appendix. For the circular and square (*b*/*a* = 1) ring-bar structures the phase velocity and frequency range of operation are close to each other since the period and cross section perimeter are the same for both structures. Similar to the PH-SEC, the RRB-SEC with square cross section tends to have slightly faster phase velocity and higher interaction impedance than that for the circular cross section due to strong field coupling at the four right angle corners. For the RRB-SEC with cylindrical vias, the dimensions of the vias and ring pads are greater than that of the tape vias; hence, there is a slight difference in the phase velocity and the interaction impedance for the two cases. In addition, the phase velocity and interaction impedance for the circular and square ring-bar structure are greater than that for the

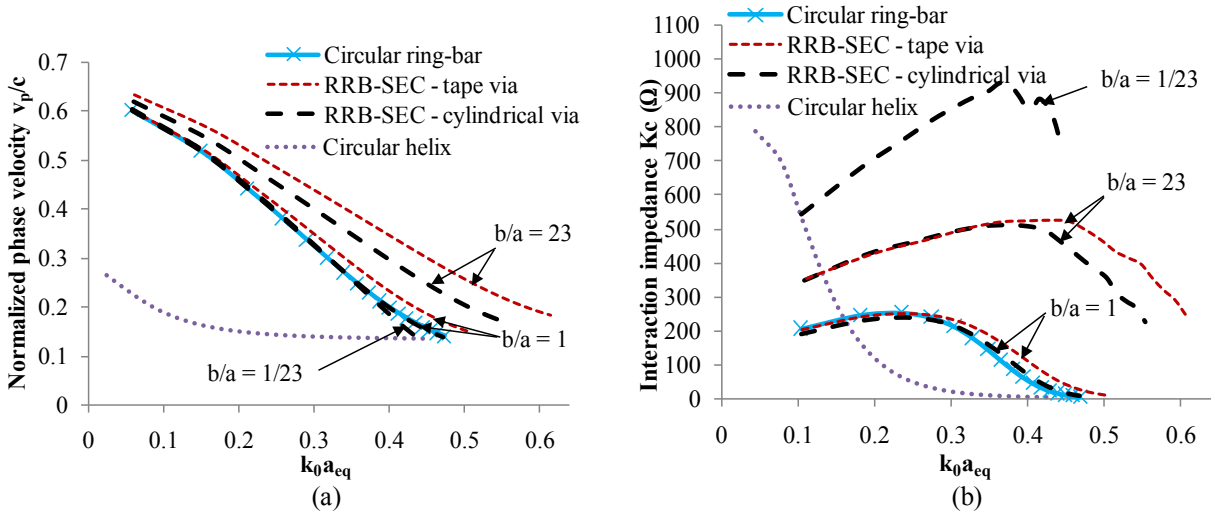


Fig. 6 Simulated (a) normalized phase velocity and (b) interaction impedance for circular helix, circular ring-bar and RRB-SEC for $b/a$ = 1, 23 and 1/23 with fixed $P$ and $L$.

circular helix.

Unlike the circular ring-bar structure, the RRB-SEC allows an additional degree of freedom with respect to the aspect ratio $b/a$. For $b/a$ = 23, the phase velocity, interaction impedance and bandwidth are greater than that for the square RRB-SEC. This effect is similar to that for the rectangular helix and PH-SEC (see Fig. 3), since the RRB-SEC is a combination of two PH-SECs. For $b/a$ = 1/23, the phase velocity does not change much compared to that for the square case; however, interestingly, the interaction impedance is significantly greater than that for $b/a$ = 23. The reason for this is that for $b/a$ = 1/23, the straight-edge connections (along the $x$-direction) in a particular ring are quite close to each other with the current flow in the same direction. This effect does not occur in the case of the PH-SEC with $b/a$ = 1/23; for the PH-SEC the current flow in the straight-edge connections (along the $x$-direction) in a particular turn is in opposite directions and therefore, unlike the RRB-SEC, there is no build up of a strong axial electric field.

Figure 7 shows the phase velocity and interaction impedance for the fundamental forward and backward waves for the RRB-SEC with cylindrical vias, with $b/a$ = 1 and 23. Two results for the square PH-SEC with cylindrical vias, with $P/L$ = 3.14 and 2.511, are also plotted in this figure. The dimensions of the PH-SEC are selected so that the phase velocity values of the fundamental forward wave of the PH-SEC and the RRB-SEC coincide at $k_0a_{eq}$ = 0.3. The ratio of the backward- to- forward impedance for both cases of the PH-SEC is ~19 % at $k_0a_{eq}$ = 0.3. For the RRB-SEC, this ratio is much lower, being 0.84% and 0.22% for $b/a$ = 1 and 23, respectively.

### 3.2 Effect of dimensional parameters

As the frequency increases, the effect of even small changes in the dimensions may be significant. In this sub-section, we study the effect of variations in $L$, $ST$, $SW$, $BW$, and $VD$ (together with $RD$) on the phase velocity and interaction impedance for the RRB-SEC with cylindrical vias, in free space. The detailed dimensions of each structure are listed in Table 2 in

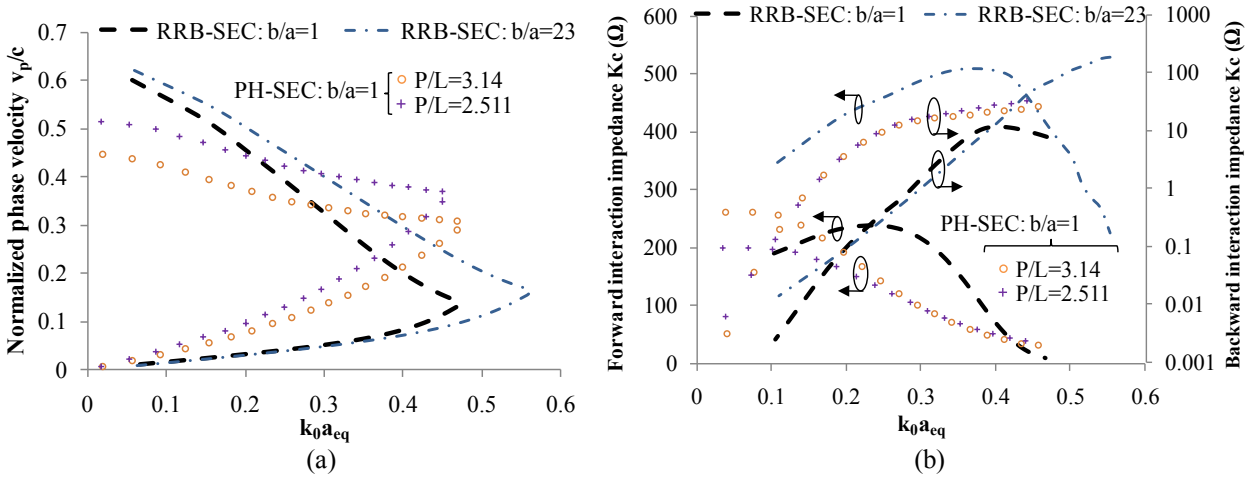


Fig. 7 Simulated (a) normalized phase velocity and (b) interaction impedance for the RRB-SEC with cylindrical vias for the fundamental forward and backward waves for $b/a$ = 1 and 23. Results for the PH-SEC with cylindrical vias, with $P/L$ = 3.14 and 2.511 for $b\ a$ = 1, are also included.

the Appendix. In general, the nature of these effects is similar to that reported for the circular ring-bar structure [26] and [35].

Figure 8 shows the phase velocity and interaction impedance for the RRB-SEC with different values of the period $L$, for $b/a$ = 1 and 23. For a given perimeter, the period mainly controls the phase velocity. As the period increases, the phase velocity increases and the bandwidth reduces. The interaction impedance may increase or decrease as the period increases depending on whether the frequency range is below or above a certain 'cross-over frequency'. A similar effect has also been observed in [35] for the circular ring-bar structure. The cross-over frequency is shifted to the band-edge for $b/a$ = 23.

The effect of different values of the bar width $BW$ on the phase velocity and interaction

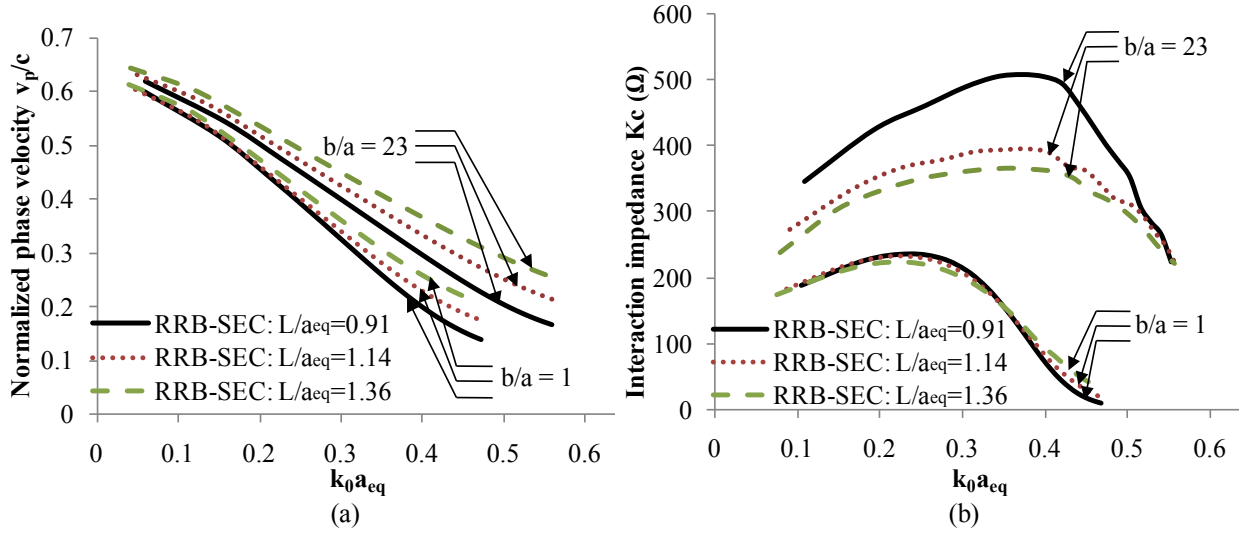


Fig. 8 Simulated (a) normalized phase velocity and (b) interaction impedance for the RRB-SEC with cylindrical vias, with different values of the period $L$ for $b/a$ = 1 and 23.

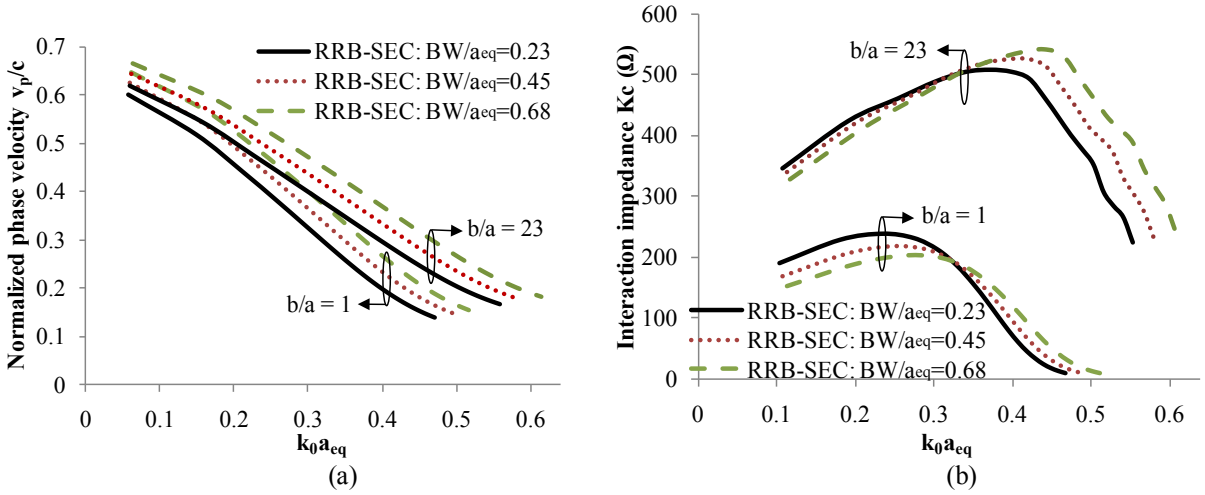


Fig. 9 Simulated (a) normalized phase velocity and (b) interaction impedance for the RRB-SEC with cylindrical vias, with different values of the bar width *BW* for *b*/*a* = 1 and 23.

impedance for *b*/*a* = 1 and 23 is shown in Fig. 9. As the bar width increases, the current can have a shorter path to move from one ring to the next, having the same effect as reducing the perimeter for a given period. As a result, the phase velocity and bandwidth increase as the bar width increases. A similar effect for the circular ring-bar structure was reported in [26]. Similar to the effect of the period in the previous figure, the interaction impedance may increase or decrease as the bar width increases, depending on whether the frequency range is below or above a certain 'cross-over frequency'.

The effects of varying the strip thickness *ST*, strip width *SW*, and via-diameter *VD* on the phase velocity and interaction impedance are shown in Figs. 10, 11 and 12, respectively. Figure 10 shows that the phase velocity for thicker metal strips is higher at low frequencies and becomes lower above a certain cross-over frequency. The interaction impedance of the fundamental

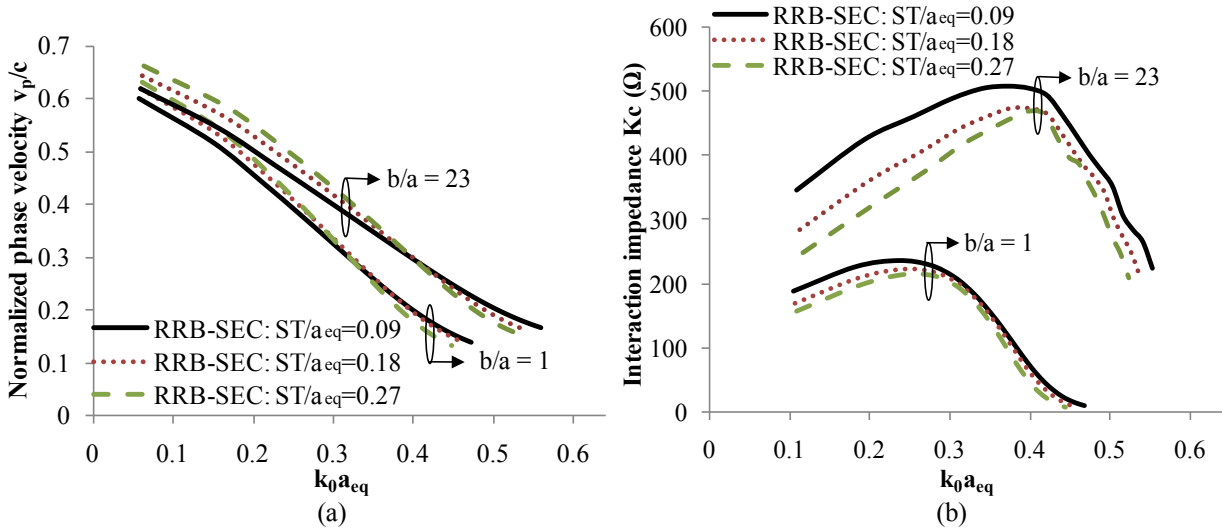


Fig. 10 Simulated (a) normalized phase velocity and (b) interaction impedance for the RRB-SEC with cylindrical vias, with different values of the metal strip thickness *ST* for *b*/*a* = 1 and 23.

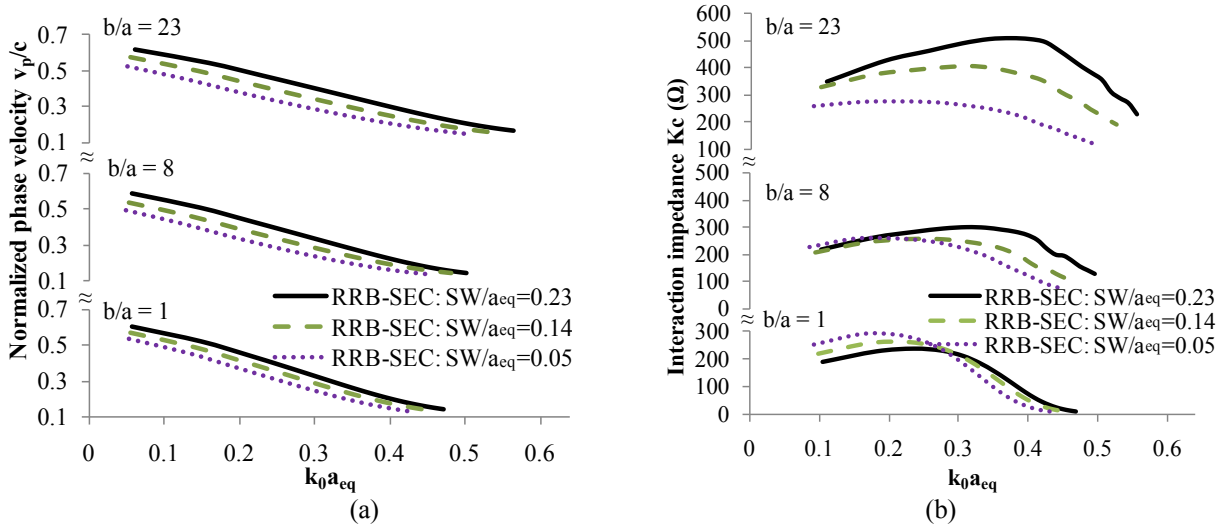


Fig. 11 Simulated (a) normalized phase velocity and (b) interaction impedance for the RRB-SEC with cylindrical vias, with different values of the strip width *SW* for *b*/*a* = 1, 8 and 23.

forward wave decreases for thicker metal strips due to an increase in the stored energy [26]. As shown in Fig. 11, the phase velocity and bandwidth decrease as the strip width decreases. The strength of interaction impedance may increase or decrease for different strip widths. As shown in Fig. 11 (b), as the aspect ratio increases, the interaction impedance cross-over frequency shifts towards lower frequencies. The effect of change of via diameter is shown in Fig. 12. For *b*/*a* = 1, the effect of variation of via diameter is similar to that of varying the strip thickness. For *b*/*a* = 23, the variation of interaction impedance does not show a clear pattern. However, an important observation is that the highest value of the interaction impedance occurs when the via-diameter matches the strip width.

### 3.3 Configurations for microfabrication of the RRB-SEC on a silicon substrate

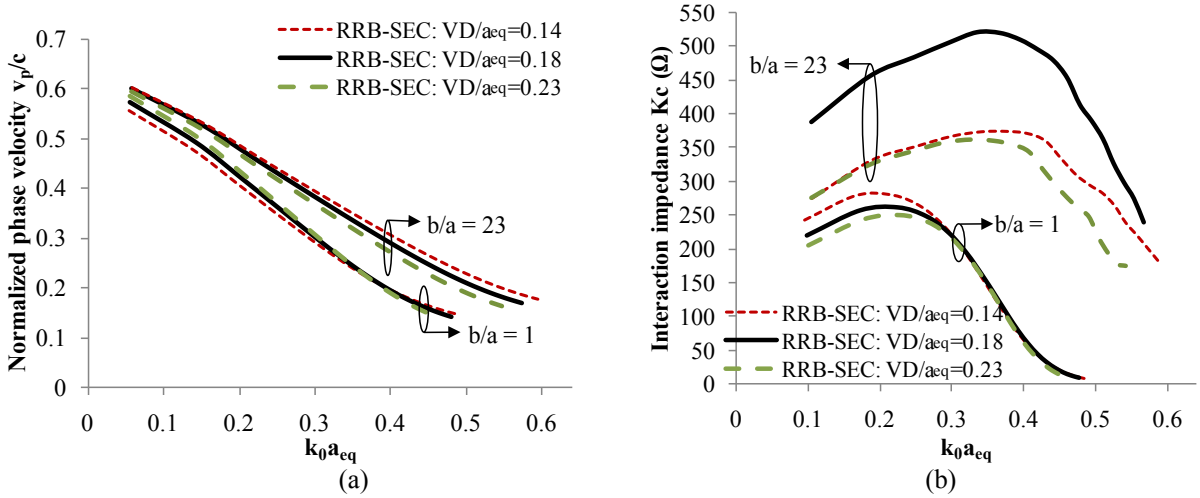


Fig. 12 Simulated (a) normalized phase velocity and (b) interaction impedance for the RRB-SEC with cylindrical vias, with different values of the via diameter *VD* for *b*/*a* = 1 and 23. *RD*/*VD* is fixed at 1.4.

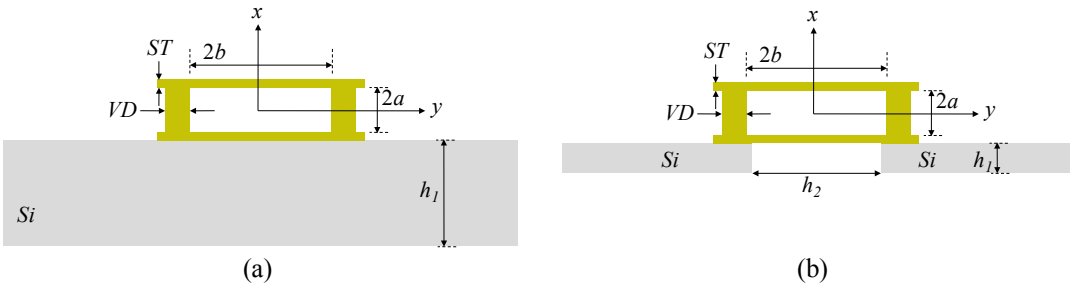


Fig. 13 Cross-sectional view of the RRB-SEC with cylindrical vias on (a) a thick silicon substrate and (b) a thin silicon substrate with a trench.

The cross-section views of the RRB-SEC with cylindrical vias, on a thick silicon substrate and on a thin silicon substrate with trench, are shown in Figs. 13 (a) and (b), respectively. Silicon has a dielectric constant of 11.9. The metal shield, used in simulations, is not shown in this figure since the shield is assumed to be placed far away from the structure. In addition, for simplicity, the effect of a thin layer of silicon dioxide ($SiO_2$), usually deposited on a silicon wafer for enhancing the eletrical insulation, is ignored. Similar to the microfabrication of PH-SEC [15] and [32], both the configurations shown in Fig. 13 can be microfabricated relatively easily since, unlike the case with many other structures shown in Table I, the fabrication process does not require bonding of two halves of the structure. The configuration with thick silicon suffers from the effect of dielectric loading and an asymmetric field distribution. Such an asymmetry may cause problems such as mode competition and gain loss in actual tube operation. The configuration with a trench in silicon (Fig. 13 (b)) reduces such problems; of course this configuration requires additional silicon etching steps.

The phase velocity and interaction impedance for both RRB-SEC configurations mentioned above, with cylindrical vias and $b/a$ = 1 and 23, are shown in Fig. 14. Both structures are assumed to have an identical $P/L$ ratio; $h_1$ for the thick silicon case is 350 $\mu m$; $h_1$ and $h_2$ for the case of trench in silicon are 50 $\mu m$ and 220 $\mu m$, respectively. Other dimensions of each structure can be found in Table 2 in the Appendix. As expected, due to dielectric loading, the bandwidth and phase velocity for the thick silicon configuration is lower than that for the trench in silicon. The interaction impedance values at $x = -a/2$, 0 and $a/2$, $y = 0$ (see Fig. 13), for $b/a$ = 1 and 23 are plotted in Figs. 14 (b) and (c), respectively. For the thick silicon configuration, the variation in the interaction impedance along the $x$-axis is asymmetric, with generally higher values for the negative values of $x$ for both aspect ratios. On the other hand, for the trench in silicon configuration, the interaction strengths at $\pm a/2$ are relatively more uniform. The uniformity is much better for the high aspect ratio structure since the silicon is far away from the center of the structure; in addition, the interaction impedance at the centre of the structure also increases compared to the thick silicon case.

## 4. Microfabrication of w-band RRB-SEC with CPW feed

In this section, we present the design, microfabrication, and measurement of the RRB-SEC with CPW feed at W-band. For this proof-of-concept fabrication, we choose the configuration with a thick silicon substrate (Fig. 13 (a)), with the standard thickness of 750 $\mu m$, due to simpler

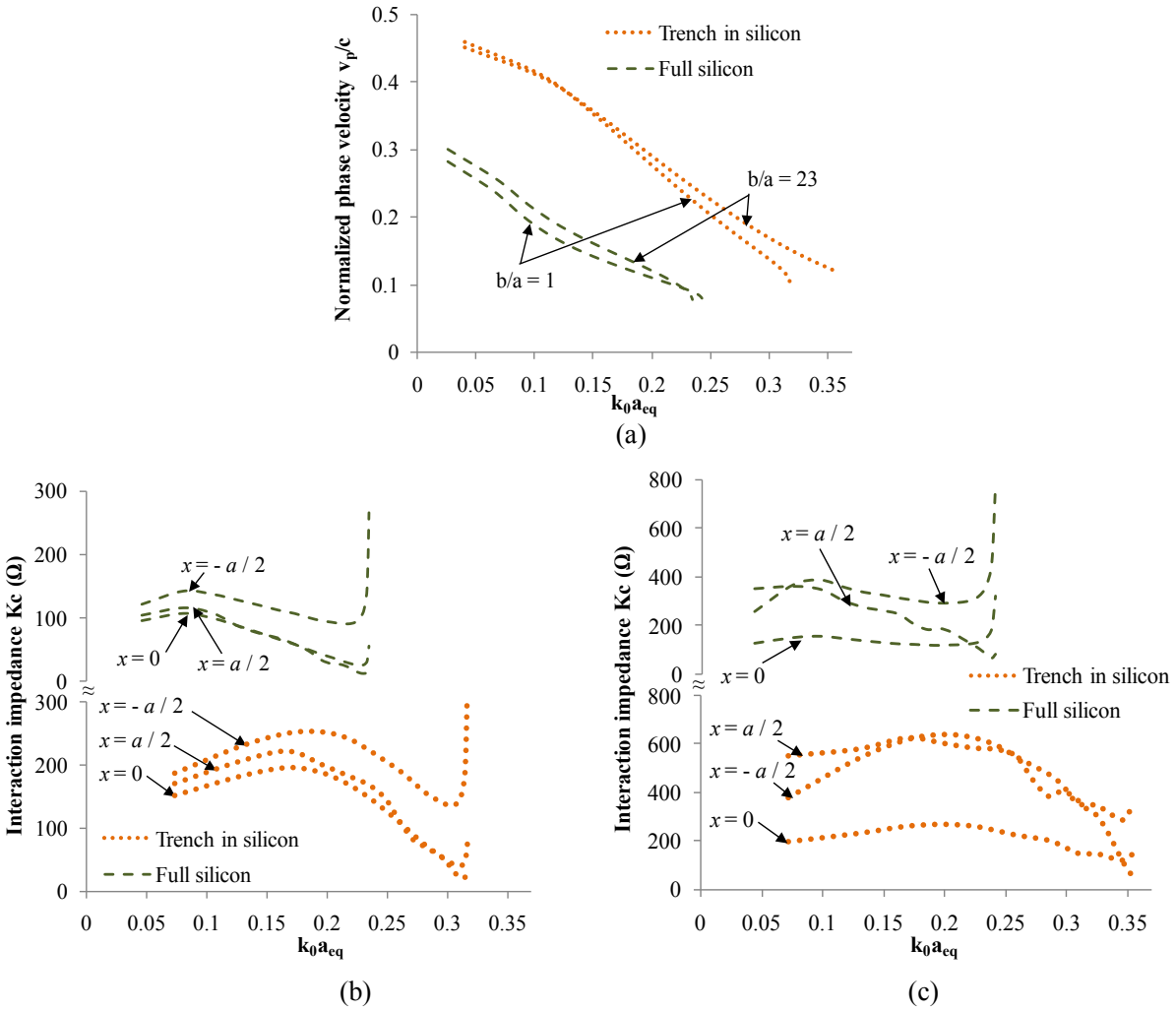


Fig. 14 Simulated (a) normalized phase velocity and interaction impedance for the RRB-SEC with cylindrical vias for (b) $b/a = 1$ and (c) $b/a = 23$ for the silicon configurations.

microfabrication. The fabrication process steps, as shown in Fig. 15, are the same as those for the PH-SEC described in [15] and [32]. The capability of building high density or high aspect ratio vias is also verified in this experiment. RRB-SEC structures with 22 periods, $b/a = 3.18$, $P = 368$ $\mu m$, $L = 192.85$ $\mu m$, $ST = 3$ $\mu m$, $SW = 40$ $\mu m$, $RD = 50$ $\mu m$, $VD = 40$ $\mu m$ and $BW = 40$ $\mu m$ are fabricated on an 8-inch high-resistivity silicon wafer.

The RRB-SEC with CPW feed is designed using CST Microwave Studio. A CPW section starts from the bottom of the first rectangular ring, as shown in Fig. 15 (a), followed by a tapered section, with a taper length of 595 $\mu m$, to join a 50 Ω section. To ensure the excitation of the symmetric mode, the signal line of the CPW with width 40 μm is centered at $y = 0$ (see Fig. 13). The edge of the CPW ground planes is 31 $\mu m$ away from the edge of the vias along the $z$-direction. The length of the tapered CPW section and the impedance of the initial CPW section are important parameters to achieve good impedance matching.

Figure 15 shows the cross-section view of the three major stages of fabrication of the

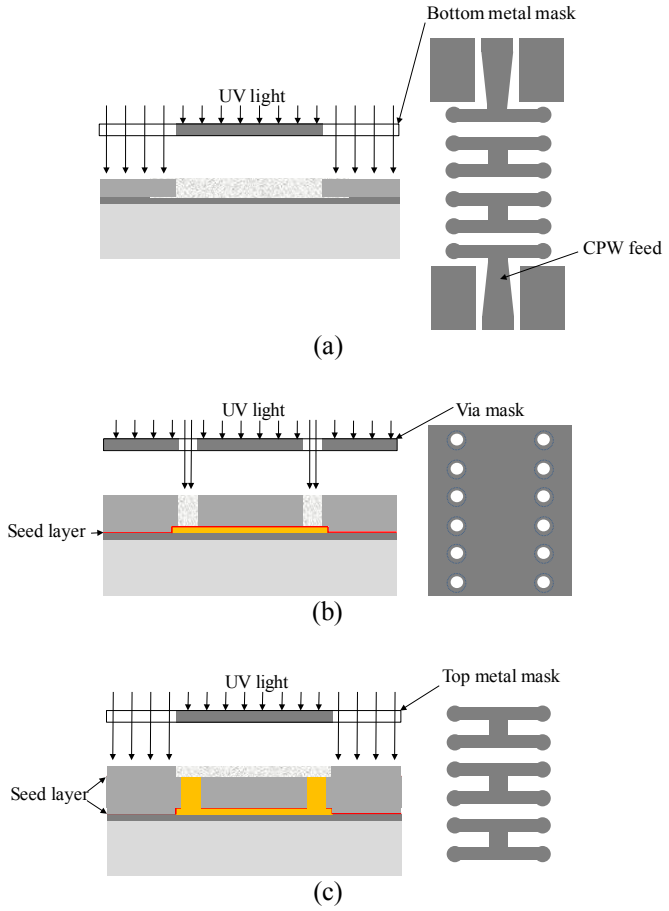


Fig. 15 Fabrication process steps for the RRB-SEC with cylindrical vias: (a) bottom Cu lift-off, (b) first seed layer deposition followed by patterning and electroplating of Cu vias, (c) second seed layer deposition followed by patterning and electroplating of Cu helix bridges.

RRB-SEC. A 3 $\mu m$ $SiO_2$ layer is deposited on top of the silicon wafer. The bottom metal layer and CPW feeds, as shown in Fig. 15 (a), are formed using the negative tone photoresist MaN-1440 lift-off process. Figure 15 (b) shows the vias formed by lithography of a thick positive tone photoresist layer (AZ 40XT-11D) and subsequent electroplating. A layer of negative tone dry film photoresist, as shown in Fig. 15 (c), is laminated and patterned to form the electroplating mold for the suspended rectangular ring bridges. Finally, the structure is released through several wet immersions in the photoresist strippers and Cu/Ti etchants. More details of the fabrication process, such as spin speed, bake temperature, bake time, exposure energy, etc. can be found in [15]. This process can be easily scaled to fabricate an RRB-SEC with higher aspect ratio and higher frequency. The dimensions of the successfully fabricated structures are measured using a profiler and a scanning electron microscope (SEM). The SEM micrographs of the successfully fabricated RRB-SEC are shown in Fig. 16. Thickness of the bottom and top horizontal metal layers is 2.38 $\mu m$ and 3.8 $\mu m$, respectively. The surface roughness for the fabricated structures is measured using an atomic force microscope (AFM). The root-mean-square (rms) roughness value for the bottom metal layer (based on the lift-off process) is 13.65 *nm*, while the rms roughness for the top bridges layer (based on the electroplating process) is 143.40 *nm*. Details of the other dimensions are the same as those reported in [32]. Considering that the skin depth for bulk

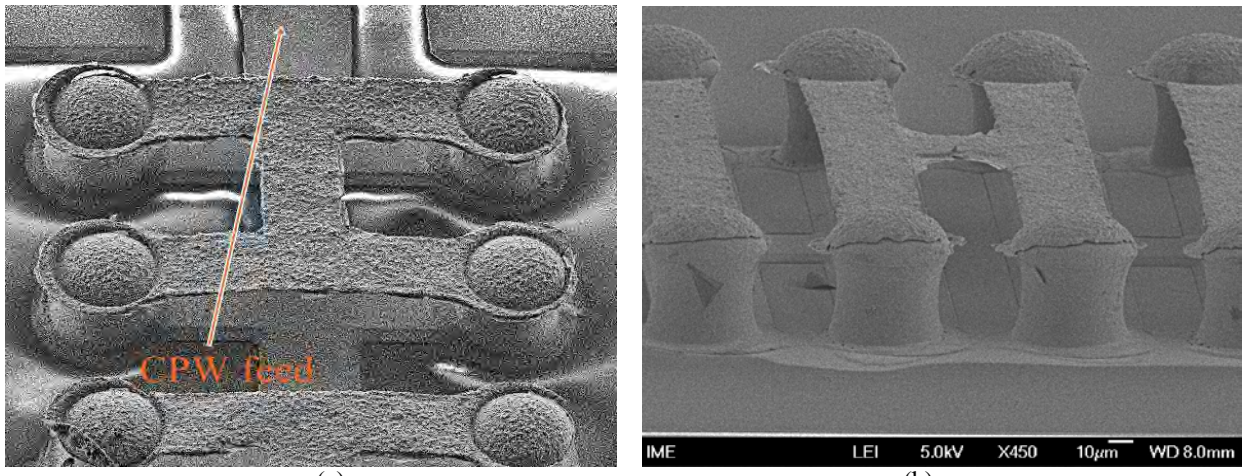


(a) (b)

Fig. 16 SEM micrographs of the fabricated RRB-SEC structure. (a) Bird's-eye view showing the RRB-SEC, with cylindrical via, with CPW feed. (b) Side view of the electroplated vias showing the convex profile at the top.

copper at 100 *GHz* is 210 *nm*, the additional loss due to the surface roughness for the bottom metal layer is very small. However, the surface roughness of the top bridges layer is significant in terms of skin depth and can cause a considerable increase in the conductor loss.

The cold-test properties of the RRB-SEC with different structure dimensions have been presented in sub-section 3.1. To maintain high interaction impedance, the strip thickness should be kept to as low a value as possible. However, the top surface of the vias has a convex profile, as shown in Fig. 16 (b), due to non-uniform rate of electroplating. The convex profile causes difficulty for the connections between the vias and the rectangular ring bridges. A firm connection between the vias and the helix bridges is mainly determined by the via height. To achieve good connections and maintain the thickness of the suspended bridges at a low value, 3 $\mu m$ in this case, the vias need to be over-plated so that most of the convex portion is above the mold. The convex portion can be removed by an additional step of polishing. However, we continue to build the rectangular ring bridges without removing the convex portion since the over-plated region is relatively small and it does not affect the subsequent process steps.

Fig. 17 shows a comparison of the measured and simulated *S*-parameters for the fabricated RRB-SEC structures. In simulations, the effective conductivity of the three metal layers is modified to take into account the surface roughness, following the models proposed in [32]. The effective conductivities of the bottom horizontal metal layer, via layer and the top horizontal metal layer, are 5.75E7 *s* / *m*, 3E4 *s* / *m* and 4E6 *s* / *m*, respectively. The results demonstrate that the RRB-SEC structure with a CPW feed has a wide -20 *dB* $S_{11}$ bandwidth, covering the frequency range from 80 *GHz* to 110 *GHz*. The simulated $S_{21}$ results agree well with the measured result since the effect of surface roughness and contact resistance are considered in the simulation. The deviation from the measured results is mainly attributed to the dimensional errors arising during the fabrication. The measured $S_{21}$ for a 22 turn-PH-SEC with an identical cross section perimeter, but a different period *L* (152.85 $\mu m$) [32], is also included. It is seen that the RRB-SEC has an insertion loss similar to that for the PH-SEC. However, as shown in Section 3, compared to the PH-SEC, the RRB-SEC should be more suitable for high power operation.

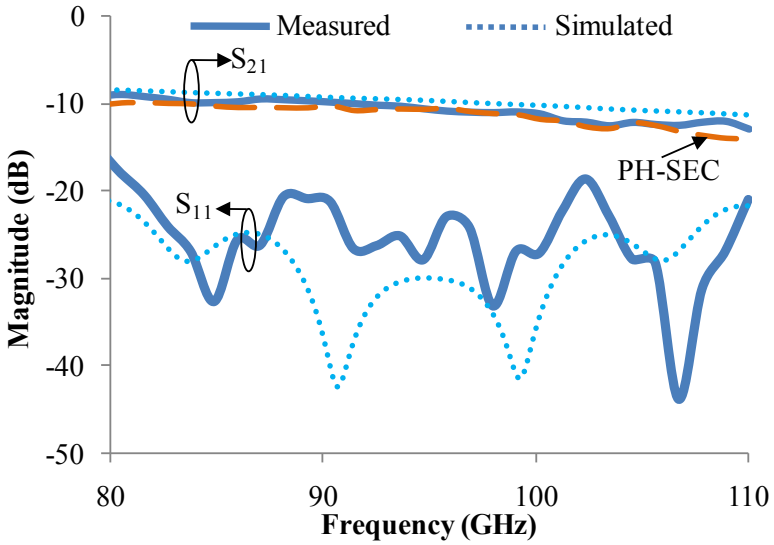


Fig. 17 Measured and simulated *S*-parameters for the fabricated RRB-SEC with cylindrical via. The surface roughness and contact resistance have been accounted as effective conductivity [32] for each metallization layers during simulation. Measured $S_{21}$ of PH-SEC with identical cross section perimeter is included for comparison.

## 5. Conclusion

In this paper, first of all, a brief summary of some of the recently proposed SWSs for application in THz VEDs has been presented; the microfabrication techniques used in the fabrication of these structures have also been mentioned. This is followed by description of two planar helical SWSs, which are the planar analogs of the circular helix and the circular ring-bar structures. Both planar structures can be designed for operation with a sheet electron beam. For the first of these structures, the PH-SEC, through the results on dispersion characteristics and interaction impedance, it has been shown that the ratio of the interaction impedance for the backward- and forward-wave can be rather high. This may adversely affect the high power operation of a TWT incorporating the PH-SEC. To solve this problem, a new planar structure, the RRB-SEC, has been proposed and investigated in detail. It has been demonstrated that the dispersion and interaction impedance properties of the RRB-SEC are very similar to those for the circular ring-bar structure. Thus, the ratio of the interaction impedance for the backward- and forward-wave for the RRB-SEC is significantly less than that for the corresponding circular tape helix and PH-SEC. The studies have also shown that the interaction impedance for the RRB-SEC increases for thin horizontal metal strips and when the via diameter matches the strip width. Two configurations for the RRB-SEC which can be microfabricated on a silicon substrate have also been presented. The simpler of these two configurations has been designed for operation at W-band and fabricated on a high-resistivity silicon wafer. It has been shown that the measured cold-test *S*-parameters match well with the simulation results. The structures and microfabrication process presented here are expected to be easily scalable for operation at THz frequencies using cylindrical or sheet electron beam.

## Acknowledgment

This work was supported by the Science and Engineering Research Council of A*STAR (Agency for Science, Technology and Research), Singapore. The grant number for the project is 082 141 0040. The authors thank Mr. Ho Soon Wee, Mr. James Toh, Mr. Zulkiflee, and Mr. Lee Yong Hean for their support in the fabrication process and Dr. Wang Lei for his kind support in *S*-parameters measurement.

## Appendix

Tab. 2 SUMMARY OF STRUCTURE DIMENSIONS IN THE VARIOUS FIGURES ($\mu m$)

| Fig. | Description | *P* | *L* | *ST* | *SW* | *RD* | *VD* | *BW* |
|---|---|---|---|---|---|---|---|---|
| 3 | Circular helix | 1382.4 | 200 | 20 | 50 | - | - | - |
| | Rectangular helix | 1382.4 | 200 | 20 | 50 | - | - | - |
| | PH-SEC (tape via) | 1382.4 | 200 | 20 | 50 | - | - | - |
| | PH-SEC (cylindrical via) | 1382.4 | 200 | 20 | 50 | 70 | 50 | - |
| 4 | PH-SEC (cylindrical via) | 691.2 | 100 | 20 | 50 | 70 | 50 | - |
| | PH-SEC (cylindrical via) | 2748 | 700 | 20 | 50 | 70 | 50 | - |
| | PH-SEC (cylindrical via) | 691.2 | 100 | 20 | 50 | 70 | 50 | - |
| 6 | Circular ring-bar | 1382.4 | 200 | 20 | 50 | - | - | 50 |
| | RRB-SEC (tape via) | 1382.4 | 200 | 20 | 50 | - | - | 50 |
| | RRB-SEC (cylindrical via) | 1382.4 | 200 | 20 | 50 | 70 | 50 | 50 |
| | Circular helix | 1382.4 | 200 | 20 | 50 | - | - | - |
| 7 | RRB-SEC (cylindrical via) | 1382.4 | 200 | 20 | 50 | 70 | 50 | 50 |
| | PH-SEC (cylindrical via) | 2260 | 900 | 20 | 50 | 70 | 50 | - |
| | PH-SEC (cylindrical via) | 2512 | 800 | 20 | 50 | 70 | 50 | - |
| 8 | RRB-SEC (cylindrical via) | 1382.4 | 200 | 20 | 50 | 70 | 50 | 50 |
| | RRB-SEC (cylindrical via) | 1382.4 | 250 | 20 | 50 | 70 | 50 | 50 |
| | RRB-SEC (cylindrical via) | 1382.4 | 300 | 20 | 50 | 70 | 50 | 50 |
| 9 | RRB-SEC (cylindrical via) | 1382.4 | 200 | 20 | 50 | 70 | 50 | 50 |
| | RRB-SEC (cylindrical via) | 1382.4 | 200 | 20 | 50 | 70 | 50 | 100 |
| | RRB-SEC (cylindrical via) | 1382.4 | 200 | 20 | 50 | 70 | 50 | 150 |
| 10 | RRB-SEC (cylindrical via) | 1382.4 | 200 | 20 | 50 | 70 | 50 | 50 |
| | RRB-SEC (cylindrical via) | 1382.4 | 200 | 40 | 50 | 70 | 50 | 50 |
| | RRB-SEC (cylindrical via) | 1382.4 | 200 | 60 | 50 | 70 | 50 | 50 |
| 11 | RRB-SEC (cylindrical via) | 1382.4 | 200 | 20 | 50 | 70 | 50 | 50 |
| | RRB-SEC (cylindrical via) | 1382.4 | 200 | 20 | 30 | 70 | 50 | 50 |
| | RRB-SEC (cylindrical via) | 1382.4 | 200 | 20 | 10 | 70 | 50 | 50 |
| 12 | RRB-SEC (cylindrical via) | 1382.4 | 200 | 20 | 40 | 42 | 30 | 50 |
| | RRB-SEC (cylindrical via) | 1382.4 | 200 | 20 | 40 | 56 | 40 | 50 |
| | RRB-SEC (cylindrical via) | 1382.4 | 200 | 20 | 40 | 70 | 50 | 50 |
| 14 | RRB-SEC (cylindrical via) | 944 | 150 | 3 | 40 | 56 | 40 | 40 |

## References

[1] R.K. Parker, R.H. Abrams, B.G. Jr. Danly and B. Levush, "Vacuum electrons"， *IEEE Trans. Microwave Theory and Techniques*, 50, 3, 835-845, (2002).

[2] J-B. Yoon, B-I. Kim, Y-S. Choi, and E. Yoon, "3-D construction of monolithic passive components for RF and

microwave ICs using thick-metal surface micromachining technology", *IEEE Trans. Microwave Theory and Techniques*, 51, 1, 279-288, (2003).

[3] S. Bhattacharjee, J. H. Booske, C. L. Kory, D. W. van der Weide, S. Limbach, S. Gallagher, J. D. Welter, M. R. Lopez, R. M. Gilgenbach, R. L. Ives, M. E. Read, R. Divan, and D. C. Mancini, "Folded waveguide traveling-wave tube sources for terahertz radiation", *IEEE Trans. Plasma Sci.*, 32, 3, 1002–1014, (2004).

[4] Y. M. Shin, J. K. So, S. T. Han, K. H. Jang, G. S. Park, J. H. Kim and S. S. Chang, " Microfabrication of millimeter wave vacuum electron devices by two-step deep-etch x-ray lithography", *Appl. Phys. Lett.*, 88, 091916, (2006).

[5] R. Zheng, W. Sun and X. Chen, "Characterizing and smoothing of striated sidewall morphology on UV-exposed thick SU-8 structures for micromachining millimeter wave circuits", *J. Micromech. Microeng.*, 20, 3, (2010).

[6] Y. M. Shin, G. S. Park, G. P. Scheitrum and B. Arfin, "Novel coupled-cavity TWT structure using two-step LIGA fabrication", *IEEE Trans. Plasma Sci.*, 31, 6, 1317-1324, (2003).

[7] C. W. Baik, Y. M. Son, S. I. Kim, S. C. Jun, J. S. Kim, J. S. Hwang; J. M. Kim, S. W. Moon, H. J. Kim, J. K. So, G. S. Park, "Microfabricated coupled-cavity backward-wave oscillator for terahertz imaging", *IEEE Int. Vacuum Electron. Conf.*, 398, (2008).

[8] O. Kwon, J. K. So, A. Srivastava, M. Sattorov, R. K. Barik, A. Bera, A. K. Tanwar, S. H. Park, I. K. Baik, J. H. Choi, J. Kim, J. W. Yang, J. H. Kim, S. S. Chang, G. S. Park, "Micro-fabricated millimeter wave vacuum electron devices", *Int. Conf. on Infrared, Millimeter, and Terahertz Waves*, pp. 2, (2010).

[9] L. Earley, B. Carlsten, F. Krawczyk, J. Potter, F. Sigler, E. Smirnova, R. Wheat, C. Heath and A. Bailey, "Wideband RF structure for millimeter wave TWTs", *AIP Conference Proceedings*, 807, 335-341, (2006).

[10] Y. M. Shin, L. R. Barnett, D. Gamzina, N. C. Luhmann, Jr., M. Field and R. Borwick, "Terahertz vacuum electron circuits fabricated by UV lithographic molding and deep reactive ion etching", *Appl. Phys. Lett.*, 95, 181505, (2009).

[11] C. Paoloni, F. Brunetti, A. Di Carlo, M. Mineo, E. Tamburri, M.L.Terranova, G. Ulisse, A. Durand, R. Marchesin, K. Pham, V. Krozer, M. Kotiranta, A. de Rossi, D. Dolfi, P. Guiset, P. Legagneux, J.P. Schnell, A. Fiorello, M. Dispenza, A. Secchi, V. Zhurbenko, S. Megtert, F. Bouamrane, C.-S. Cojocaru, A. Gohier, "The OPTHER project: progress toward the THz amplifier", *IEEE Int. Vacuum Electron. Conf.,* Bangalore, India, pp. 55-56, (2011).

[12] S. Sengele, H. Jiang, J. H. Booske, C. Kory, D. van der Weide and L. Ives, "Microfabrication and characterization of a selectively metallized W-band meander-line TWT circuit", *IEEE Trans. on Electron Devices*, 56, 5, 730-737, (2009).

[13] M. R. Lueck, D. M. Malta, K. H. Gilchrist, C. L. Kory, G. T. Mearini and J. A. Dayton, Jr., "Microfabrication of diamond-based slow-wave circuits for mm-wave and THz vacuum electron sources", *J. Micromech. Microeng.*, 21, 6, 065022, (2011).

[14] J. A. Dayton, Jr., C. Kory, G. Mearini, D. Malta, M. Lueck, and K. Gilchrist, "Applying microfabrication to helical vacuum electron devices for THz applications", *IEEE Int. Vacuum Electron. Conf.*, (2009).

[15] C. Chua, J. Tsai, M. Tang, S. Aditya and, Z. Shen, "Microfabrication of a planar helix with straight-edge connections slow-wave structure", *Advanced Materials Research*, 254, 17-20, (2011).

[16] M. J. Madou, "Fundamentals of microfabrication: the science of miniaturization", CRC Press, NewYork, (1997).

[17] R. L. Ives, "Microfabrication of high-frequency vacuum electron devices", *IEEE Trans. Plasma Sci.*, 32, 3, 1277-1291, (2004).

[18] C. Chua, S. Aditya, and Z. Shen, "Effective dielectric constant method for a planar helix with straight-edge connections", *IEEE Electron Device Letters*, 30, 11, 1215-1217, (2009).

[19] R. K. Arora, B. Bhat, and S. Aditya, "Guided waves on a flattened sheath-helix", *IEEE Trans. Microwave Theory and Techniques*, MTT-25, 71-72, (1977).

[20] S. Aditya and R. K. Arora, "Guided waves on a planar helix", *IEEE Trans. Microwave Theory and Techniques*, MTT-27, 860-863, (1979).

[21] C. F. Fu, Y. Y. Wei, W. X. Wang, and Y. B. Gong, "Dispersion characteristics of a rectangular helix slow-wave structure", *IEEE Trans. on Electron Devices*. 55, 12, (2008).

[22] Vishnu Srivastava, "THz vacuum microelectronic devices", *International Symposium on "Vacuum Science and Technology*", 012 015, (2007).

[23] B. E. Carlsten, S. J. Russell, L. M. Earley, F. L. Krawczyk, J. M. Potter, P. Ferguson, and S. Humphries, "Technology development for a mm-wave sheet-beam TWT", *IEEE Trans. Plasma Sci*., 33, 1, 85–93, (2005).

[24] S. J. Cooker, B. Levush and T. M. Antonsen, Jr., "A coupled-cavity slow-wave structure for sheet-beam devices", *IEEE Int. Vacuum Electron. Conf*., 487-488, (2006).

[25] M. Chodorow and E. L. Chu, "Cross-wound twin helices for traveling wave tubes", *J. Appl. Phys*., 26, 1, 33–43, (1955).

[26] C. K. Birdsall and T. E. Everhart, "Modified contra-wound helix circuits for high-power traveling-wave tubes", *IRE Trans. Electron Devices*, 3, 4, 190–204, (1956).

[27] C. Chua, S. Aditya, and Z. Shen, "Planar helix with straight-edge connections in the presence of multilayer dielectric substrates", *IEEE Trans. on Electron Devices*, 57, 12, 3451-3459, (2010).

[28] C. Chua, S. Aditya and, Z. Shen, "Planar helix slow-wave structure with straight-edge connections", PCT/SG2010/000152, (2010).

[29] C. Chua, S. Aditya, Z. Shen, M. Tang, and J. Tsai, "Planar helix with straight-edge connections and a sheet electron beam for traveling-wave tube applications", *IEEE Int. Vacuum Electron. Conf*., Bangalore, India, 519-520, (2011).

[30] M. Kotiranta, V. Krozer and V. Zhurbenko, "Square helix TWT for THz frequencies", *35th Int. Conf. on Infrared Millimeter and Terahertz Waves (IRMMW-THz)*, Rome, Italy, (2010).

[31] M. Kotiranta and V. Krozer, "Harmonic distortion in a traveling wave tube at 850 GHz and its use in frequency multiplication", *Workshop on Integrated Nonlinear Microwave and Millimetre-Wave Circuits (INMMIC)*, 1-4, (2011).

[32] C. Chua, J. Tsai, S. Aditya, M. Tang, S. W. Ho, Z. Shen and L. Wang, "Microfabrication and characterization of W-band planar helix slow-wave structure with straight-edge connections", *IEEE Trans. on Electron Device*, 58, 11, (2011).

[33] E. A. Ash, A. Pearson, A. W. Horsley, and J. Froom, "Dispersion and impedance of dielectric-supported ring-and-bar slow-wave circuits", *Proc. Inst. Elect. Eng*., 111, 4, 629–641, (1964).

[34] W. N. Cain and R. W. Grow, "The effects of dielectric and metal loading on the dispersion characteristics for contrawound helix circuits used in high-power traveling-wave tubes", *IEEE Trans. Electron Devices*, 37, 6, 1566–1578, (1990).

[35] D. T. Lopes and C. C. Motta, "Characterization of ring–bar and contrawound helix circuits for high-power travelling-wave tubes", *IEEE Trans. Electron Devices*, 55, 9, 2498–2504, (2008).

[36] S. K. Datta, V. B. Naidu, P. R. R. Rao, L. Kumar, B. N. Basu, "Equivalent circuit analysis of a ring–bar slow-wave structure for high-power traveling-wave tubes", *IEEE Trans. Electron Devices*, 56, 12, 3184–3190, (2009).

[37] S. S. Rajan and J. A. Dayton, Jr., "Method for fabricating three dimensional traveling wave tube circuit elements using laser lithography", US Patent application 6584675, (2003).

[38] L. P. Sadwick, J. H. Chern, R. J. Hwu, J. Ren, D. Wu and C. H. Lin, "Method of micro-fabrication of a helical slow wave structure using photo-resist processes", US Patent application 7504039, (2009).

[39] J. Dayton, Jr., G. T. Mearini, H. Chen and C. L. Kory, "Diamond-studded helical traveling wave tube", *IEEE Trans. Electron Devices*, 52, 5, 695-701, (2005).